International Journal of Heat and Mass Transfer 164 (2021) 120481

Contents lists available at ScienceDirect

International Journal of Heat and Mass Transfer

journal homepage: www.elsevier.com/locate/hmt

# On the influence of thermal phenomena during cavitation through an orifice

C. Esposito [a,b,*], L. Peveroni [a], J.B. Gouriet [a], J. Steelant [b,c], M.R. Vetrano [b]

[a] von Karman Institute for Fluid Dynamics, Waterloosesteenweg 72, Sint-Genesius-Rode, Belgium
[b] KU Leuven, Celestijnenlaan 300A postbus 2421, B-3001 Heverlee, Belgium
[c] Aerothermodynamics and Propulsion Analysis Section, ESTEC-ESA, Keplerlaan 1, 2200AG Noordwijk, the Netherlands

ARTICLE INFO

*Article history:*
Received 12 June 2020
Revised 14 September 2020
Accepted 16 September 2020

*Keywords:*
Cryogenic
Cavitation
Orifice
Subcooling

ABSTRACT

Thermal properties of cryogenic fluids can profoundly change the nature of cavitation since the fluid pressure drop is not, anymore, the only driving parameter of this phenomenon.

In this research, we have conducted experiments inducing cavitation via a cylindrical orifice using Liquid Nitrogen as working fluid and exploring cavitation regimes going from bubbly cavitation to full flashing. Among others, we performed unsteady pressure measurements to derive the speed of sound during cavitation and high-speed imaging to understand the evolution of the two-phase flow along the pipe.

In our analysis we use five dimensionless numbers to describe the flow conditions upstream and downstream of the orifice, and the type of transition taking place across the orifice.

In this paper, we show that the fluid initial subcooling level $\Delta T_{sub}$ upstream of the orifice and the superheat level *Rp* of the flow downstream of the orifice are two parameters essential to take into account the metastability of the fluid. Therefore, we propose a new semi-empirical model for predicting the effect of the fluid thermal properties on cavitation. Specifically, we define a parameter $\mathcal{T}$ which, multiplied by the saturation pressure at the inlet temperature, allows us to estimate the pressure reached at the orifice to cavitate.

© 2020 Elsevier Ltd. All rights reserved.

## 1. Introduction

Cavitation is a complex mechanism due to the wide range of possible regimes and the corresponding levels of noise, vibration and void fraction produced [1–3], and its complexity further increases when cryogenic fluids are involved. For those fluids, the thermodynamic effects cannot be neglected due to their smaller vapor to liquid density ratio ($\rho_v/\rho_l$) and smaller latent heat of vaporization ($L_{vap}$) [4–6]. The liquid to gas phase transition requires heat from the surrounding liquid leading to a localized cooling process and a consequent reduction of the local vapor pressure [7].

Several authors evidenced with experiments this thermodynamic effect in the framework of engineering applications such as propulsion systems [8,9], or electronics cooling [10,11], and many of them used Liquid Nitrogen ($LN_2$). Tani and Nagashima [12] studied cavitation formed at the throat of a nozzle using both water and $LN_2$. When using $LN_2$, they observed a temperature reduction, along with a vapor fraction increase, beyond the throat of the nozzle. On the contrary, tests performed using water as working fluid showed a constant temperature during cavitation. Moreover, the observed evaporative cooling modifies the vapor bubbles shape [13,14]. Indeed, since the local vapor pressure reduces with the temperature, the local cavitation number ($\sigma$) increases. As a result, the size of the bubbles is smaller than the one observed in isothermal conditions and the bubble cloud spreads out further.

The coupling of the thermodynamic effect with turbulence enhances even more the complexity of the cryogenic cavitation. Tseng and Shyy [14] helped to reduce the uncertainty associated with the inlet turbulent quantities by using a filter-based approach to model turbulence. Niiyama et al. [15] investigated the influence of turbulence on the thermodynamic effects. On one hand, they observed that the turbulent heat transfer coefficient decreases with the cavitation number ($\sigma$) while the void fraction increases. On the other hand, an increase in the Reynolds number for the same $\sigma$ value was found to enhance the thermal transport and to lead to a higher turbulent heat transfer. Another interesting outcome of this work is the effect of the turbulent flow on the bubble growth which is usually delayed by the thermodynamic effect. However, a

* Corresponding author at: von Karman Institute for Fluid Dynamics, Waterloosesteenweg 72, Sint-Genesius-Rode, Belgium.
*E-mail address:* esposito@vki.ac.be (C. Esposito).

https://doi.org/10.1016/j.ijheatmasstransfer.2020.120481
0017-9310/© 2020 Elsevier Ltd. All rights reserved.

**Nomenclature**

*Abbreviations*

| | |
|---|---|
| *3PT* | Three Pressure Transducers technique |
| $LN_2$ | Liquid Nitrogen |
| *S1*, *S2*, *S3* | tested levels of subcooling |

*List of Subscripts*

| | |
|---|---|
| *chok* | choking |
| *conf* | confined to the pipe |
| *dw* | downstream |
| *free* | free environment |
| *iso* | isothermal |
| *l* | liquid |
| *min* | minimum |
| *mix* | mixture |
| *ori* | orifice |
| *sat* | saturation |
| *up* | upstream |
| *v* | vapor |

*List of Symbols*

| | |
|---|---|
| $A$ | correction coefficient for the speed of sound |
| $A_o$ | orifice section |
| $c$ | speed of sound |
| $C_1$, $C_2$ | constants |
| $C_d$ | orifice discharge coefficient |
| $Cp$ | specific heat |
| $D$ | pipe diameter |
| $d$ | orifice diameter |
| $E$ | elasticity |
| $e$ | pipe thickness |
| $f$ | frequency |
| $F_f$ | liquid critical pressure ratio |
| $f_s$ | sampling frequency |
| $G_{i,j}$ | cross-power spectral density |
| $\mathcal{H}$ | transfer function |
| $j$ | imaginary number |
| $Ja$ | Jakob number |
| $k$ | wavenumber |
| $L$ | generic length |
| $L_{vap}$ | latent heat of vaporization |
| $M$ | Mach number |
| $P$ | pressure |
| $P_{cri}$ | critical pressure |
| $P_{sat}$ | saturation pressure |
| $Q$ | mass flow rate |
| $\hat{Q}$ | non dimensional flow rate |
| $R^2$ | coefficient of determination |
| $Rp$ | superheat ratio |
| $S$ | surface tension |
| $s$ | orifice thickness |
| $T$ | temperature |
| $T_{cri}$ | critical temperature |
| $T_{sat}$ | saturation temperature |
| $U$ | velocity |
| $x$ | generic position |
| $\beta$ | orifice characteristic ratio |
| $\gamma$ | coherence function |
| $\Delta$ | discrepancy |
| $\Delta T_{ori}$ | temperature drop through the orifice |
| $\Delta T_{sat,dw}$ | downstream temperature degree of equilibrium |
| $\Delta T_{sub}$ | subcooling degree |
| $\nu$ | Poisson ratio |
| $\xi$ | Downstream pressure ratio |
| $\rho$ | density |
| $\sigma$ | cavitation number |
| $\omega$ | angular frequency |

large turbulence intensity can yield the opposite effect. Temperature increases in the area where bubbles are present and, consequently, their collapse is delayed.

The thermodynamic effects also influence the dynamics of the cavitating flow and the consequent cavitation regimes. Zhu et al. [16] simulated a cavitating flow of $LN_2$ over an ogive. For the first time, they observed a cavitation shedding mechanism, called Partially Shedding Mode, and characterized by the presence of two distinct cavity clouds. A primary cavity cloud keeps quasi-steady, and a secondary, smaller, intermittently forms inside the primary cavity. The Partially Shedding Mode, then, convects downstream along the wall surface and flows out with a frequency of 2500 Hz. When separation occurs, the primary cavity also becomes smaller up to sweeping away with a frequency of 250 Hz. The so-called cavitation cloud is formed. Long [17] further investigates the different stages of the thermal cavitation shedding process. He also showed that the pressure fluctuations excited by the cavitation are mainly driven by the acceleration of the cavity volume. Lee and Roh [18] examined the flow instability downstream of an orifice. They highlighted the effect of the orifice configuration and showed that a convergent orifice gives less severe pressure oscillations and, hence, reduced instability.

De Giorgi et al. [19] conducted high-speed visualizations in the restricted area of a sharp-edged orifice. They confirmed the appearance of frothy cavitation with $LN_2$ with cavity structures much finer than the one observed for water at ambient conditions. Moreover, the frequency analysis of the high-speed visualizations showed that the frequency spectrum of the downstream pressure signals has a higher energy content in the range of low frequencies (up to 100 Hz) respect to what observed for water. Hitt [20] also investigated the instability frequency of cryogenic cavitation by conducting tests with $LN_2$ and analyzing the pressure signals, at a distance of 0.64 pipe diameters downstream of the orifice, via Fast Fourier Transform. He observed that the cavitation instability, induced by the orifice, is a subharmonic of the orifice wake instability and appears around $200 - 250$ Hz.

An additional parameter to take into consideration is the level of subcooling of the cryogenic fluid upstream of the orifice. Ohira et al. [21] investigated the role played by the subcooling level of $LN_2$ on cavitation. He observed that, by increasing the degree of subcooling, cavitation changes its mode from continuous to intermittent. Moreover the produced vapor disappears immediately after the cavitation onset. In other words, subcooled conditions delay or even suppress cavitation. This characteristic behavior was also highlighted in the numerical study performed by Xue [22].

When $LN_2$ is at saturation, instead, continuous cavitation occurs as the throat pressure falls just below the saturated vapor pressure. For subcooled conditions, the maximum pressure drop between the saturation pressure and the pressure at which cavitation begins is reached at $T_{throat} \sim 74$ K. Finally, the pressure oscillations, calculated as the difference between the throat static pressure prior and during cavitation, are higher in subcooled conditions when cavitation is intermittent [21]. The experiments performed by Chen et al. [23,24] with $LN_2$ found consistency with Ohira's results. They distinguished two cavitation dynamics as $LN_2$ temperature was increasing, a quasi-isothermal mode, and a thermo-sensitive mode. When $LN_2$ was around $77 - 78$ K, a transition mode was observed.

Finally, another important parameter is the physical element inducing cavitation. In the case of an orifice, a rapid and big pres-

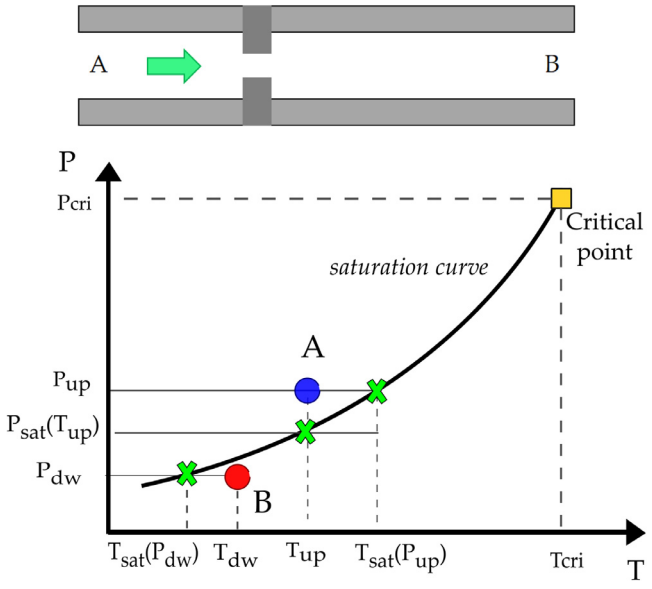


**Fig. 1.** Schematic of the flow conditions upstream (*up*) and downstream (*dw*) of the orifice respect to the saturation curve.

sure gradient is induced, therefore, non-equilibrium effects are expected. In particular, when the orifice is choking the cryogenic flow is likely to depart from thermal equilibrium since the thermal exchange between the two phases is slower than the depressurization speed [25]. A comprehensive modeling of these non-equilibrium effects is computationally expensive [26] or based on simplifications [27] and empirical parameters [28]. Therefore, homogeneous equilibrium models, even if less accurate, are often preferred in the literature [29–31].

In this context, the main goal of our paper is to evidence and to give insights to the thermal fluid properties which have a significant impact of cavitation through an orifice. For this purpose we have performed an experimental research activity, using $LN_2$ as working fluid, which includes pressure and temperature measurement at different locations upstream and downstream of the orifice, flow rate, and high-speed visualization of the flow upstream and downstream of the orifice. Our analysis aims at understanding the role played in the evolution of cavitation by five parameters: the subcooling degree ($\Delta T_{sub}$), the superheat ratio ($Rp$), the Jakob number ($Ja$), the downstream temperature degree of equilibrium ($\Delta T_{sat,\,dw}$) and the cavitation number ($\sigma$). These parameters and their physical meaning are introduced in Section 2.

The paper is further organized as follows. Section 3 describes the experimental set-up and the Three Pressure Transducers technique, Section 3.2, to derive the speed of sound. Section 4 describes the experimental results and Section 5 draws the conclusions.

## 2. Statement of the problem

The schematic in Fig. 1 presents the characteristic pressure and temperature parameters for cryogenic cavitation in a P-T phase diagram. The points A and B of the diagram represent the flow conditions upstream and downstream of the orifice, respectively. The liquid upstream of the orifice (condition A) is at a pressure $P_{up}$ and temperature $T_{up}$ above the saturation curve. How far the condition A is from saturation, in terms of temperature, determines the degree of subcooling of the liquid, see Eq. (1a). Here, the $LN_2$ critical temperature is used as reference temperature, i.e. $T_{cri} = 126.19$ K.

To induce cavitation, the condition B, with pressure $P_{dw}$ and temperature $T_{dw}$ must be located below the saturation curve. The rapid pressure drop through the orifice does not guarantee to reach in B a new thermal equilibrium condition. Thus, the distance from this equilibrium is here considered via Eq. (1b), where the temperature difference is once again nondimensionalized by dividing it by the $T_{cri}$.

The non-dimensional numbers in Eqs. (1c), (1d), and (1e) describe, instead, the way the phase change transition occurs through the orifice. In particular, the superheat level, $Rp$, defines the distance between the two-phase flow downstream of the orifice and the saturation conditions at $T_{up}$.

Since the process is not isothermal, $T_{up}$ and $T_{dw}$ can differ and temperature drops through the orifice, i.e. $\Delta T_{ori} = T_{up} - T_{dw}$. The Jakob number (Eq. (1d)) quantifies this difference, where $\rho_l$ and $\rho_v$ stand for the liquid and the vapor density, respectively, $Cp_l$ is the specific heat of the liquid phase and $L_{vap}$ is the latent heat of evaporation.

Finally, the cavitation number $\sigma$ measures the strength of the cavitation. Usually the minimum pressure $P_{min}$ in Eq. (1e) is approximated by the saturation pressure $P_{sat}$, e.g. [32], since vapor bubbles start to form when the pressure falls below the saturation and thermal effects are negligible. However, this approximation can fail for cryogenic fluids whose working conditions are closer to the critical point with respect to the case of isothermal fluids, e.g. water. Therefore, in this work, the initial definition of $\sigma$ with $P_{min}$ is maintained.

$$\Delta T_{sub} = \frac{T_{sat}(P_{up}) - T_{up}}{T_{cri}} \tag{1a}$$

$$\Delta T_{sat,dw} = \frac{T_{dw} - T_{sat}(P_{dw})}{T_{cri}} \tag{1b}$$

$$Rp = \frac{P_{sat}(T_{up})}{P_{dw}} \tag{1c}$$

$$Ja = \frac{\rho_l Cp_l \Delta T_{ori}}{\rho_v L_{vap}} \tag{1d}$$

$$\sigma = \frac{P_{up} - P_{min}}{P_{up} - P_{dw}} \tag{1e}$$

## 3. Experimental facility and methodology

### 3.1. The experimental facility

Fig. 2 shows a schematic of the cryogenic CHIEF facility [33,34], designed and manufactured at the von Karman Institute for Fluid Dynamics. $LN_2$ is stored in a ranger and can be transferred into the facility, at an adjustable and stable pressure (up to 700 kPa), via a pipeline equipped with a flowmeter and safety valves to protect against over-pressure. At maximum pressure conditions, the pressure losses through the transfer lines are about 130 kPa for a flow rate of 0.03 kg/s. These pressure losses are distributed along the line, and flow restrictions have been limited to reduce as much as possible local evaporation of the liquid phase.

The test section is a cylindrical pipe with an internal diameter D=15 mm and it is mounted upwards. It includes a cylindrical orifice of 2.5 mm diameter and two transparent sections. One is located upstream of the orifice and is 2D long (i.e. 30 mm) and the other is located downstream and is 5D long (i.e. 75 mm). These transparent modules are made of quartz and, to limit optical distortions, have plane and flame polished external surfaces. As shown in Fig. 2, the vacuum chamber, which ensures the thermal insulation of the test section from the external environment, has two viewports in correspondence of the transparent test section. High-speed imaging is performed via a Phantom v7.0 CMOS camera with a 100 mm objective and an extension tube of 30

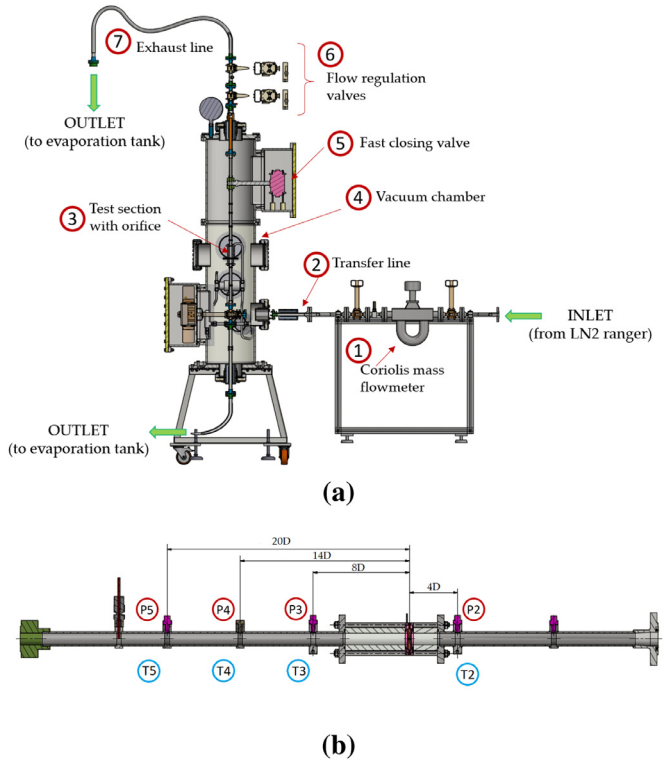


**Fig. 2.** **(a)** CHIEF facility; **(b)** particular of the test section with positioning of the pressure and temperature sensors.

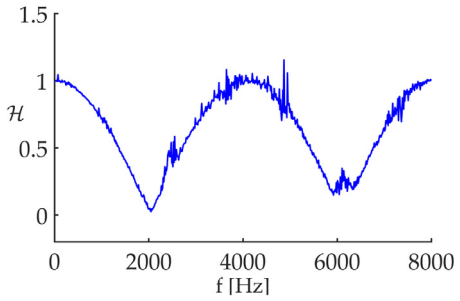


**Fig. 3.** Example of the obtained $\mathcal{H}$ function in single phase fully liquid flow with $P_{up} = 850$ kPa.

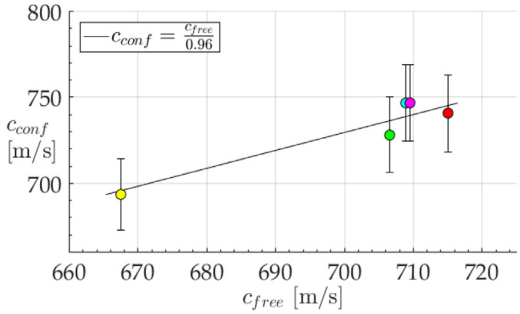


**Fig. 4.** Speed of sound in the confined volume of the pipe ($c_{conf}$) as a function of the speed of sound ($c_{free}$) in the free environment computed using the pressure and the temperature measured downstream of the orifice in fully liquid conditions.

mm. The image resolution is 288 × 560 pixels with an exposure time of 10$\mu$s at a frame rate of ~ 12 kHz. The pressure is measured along the test section with flush-mounted Kulite CTL-190M transducers having an uncertainty of ± 0.0017 MPa ± 0.4%rdg (including the thermal sensitivity shift). Measurements were acquired at 100 kHz and conditioned with a Fylde amplifier FE-H379-TA with a cut-off frequency of 30kHz. The position of these transducers, downstream of the orifice, permits to apply the Three Pressure Transducers technique [35]. The temperatures are measured at the same locations via cryogenic silicon diodes (model DT-670B-SD from Lakeshore Cryotronics Inc., with an uncertainty of ± 0.5 K). Steady conditions were averaged over ~ 2min, whereas the unsteady-state flow analysis only considers pressure measurements over 10 sec.

Experiments were conducted fixing the value of the pressure in the ranger and regulating the valve downstream of the test section to reproduce different cavitating conditions. Since the transfer line and the test section are initially at ambient temperature, a pre-cooling, the so-called chilldown, is necessary and is achieved letting $LN_2$ circulating in the pipes. This procedure was also repeated between two consecutive tests to guarantee fully liquid flow in the test section before a new operating condition is set.

### 3.2. The 3PT technique

The Three Pressure Transducers technique [35–37] allows retrieving the speed of sound in a pipe by measuring the fluctuations of the pressure waves propagating in the medium filling the pipe. At cavitation, the presence of bubbles in the flow significantly affects the speed of sound, hence, void fractions measurements are sometimes used to derive the speed of sound. However, to measure the void fraction in $LN_2$ remains problematic. In the last years, capacitive sensors have shown a great potentiality [38]. Nevertheless, these probes are impacted by thermal effects and are still in a phase of performance evaluation. Therefore, we preferred to use the 3PT technique that only depends on pressure and, applied to isothermal cavitation [39], it provided space and time average values of the speed of sound. Besides, the 3PT technique can be easily applied and this is indeed a big advantage for cryogenic applications where the thermal properties of the liquid narrow the possible techniques to apply.

The 3PT technique assumes the propagating waves to be planar and uses three unsteady pressure sensors equidistantly placed from each other. The hypothesis of one-dimensional waves implies the acoustic pressure field in the frequency domain is given by :

$$p(x, f) = C_1 e^{jkx} + C_2 e^{-jkx}, \tag{2}$$

where $k = \omega/c$ is the wavenumber, and $C_1$ and $C_2$ are two constants.

Then, by considering three sensors, i.e. the pressures $P3$, $P4$, and $P5$ in Fig. 2(b), the function $\mathcal{H}$ can be defined by combining the frequency domain representation of their measured time-varying pressure signals and it reads as:

$$\mathcal{H} = \frac{p_3 + p_5}{2p_4} = cos(k_{conf} L) = cos\left(\frac{\omega L}{c_{conf}}\right), \tag{3}$$

As shown in Fig. 3, this function reduces to a cosine, establishing, thus, a direct relation between the pressure and the speed of sound $c_{conf}$ measured in the confined volume of the pipe. In practice, to reduce random errors, the average of ten $\mathcal{H}$ functions computed from pressure signals, each recorded for 1 s acquisition time, $\overline{\mathcal{H}}$, is used.

The distance between the three sensors has to be accurately chosen to maximize the sensitivity and the robustness of the technique. In our experimental set-up, the optimal distance ($L$) was selected using the approach reported in [39] and is equal to six times the pipe diameter $D$.

The measured speed of sound ($c_{conf}$) is of course affected by the pipe properties and the fluid compressibility. Fig. 4 compares the values of $c_{conf}$ in fully liquid conditions to the $c_{free}$ calculated from the NIST database with the thermo-physical properties of the fluid

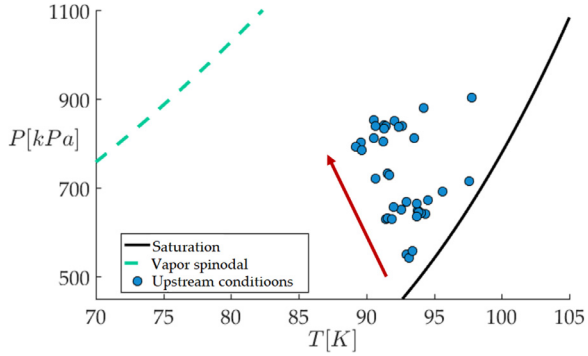


**Fig. 5.** Initial conditions of the tested cases in terms of pressure and temperature and their position in the P-T phase diagram.

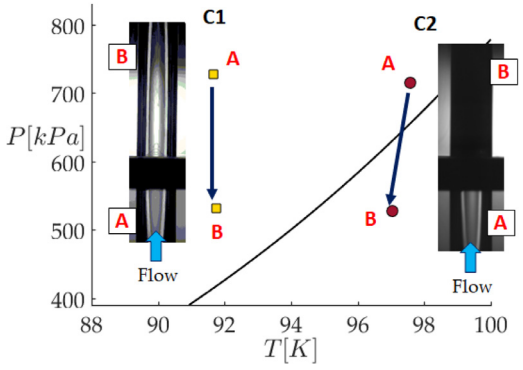


**Fig. 6.** Example of two test cases with similar $P_{up}$ and $\Delta P$.

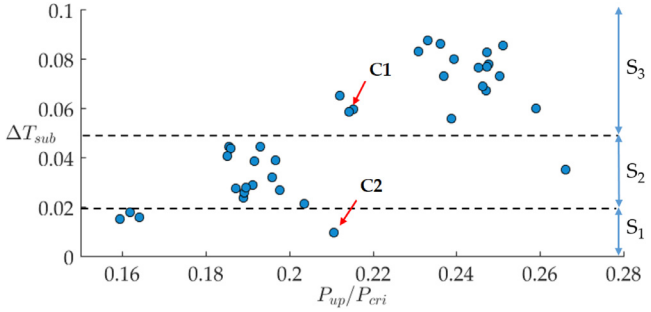


**Fig. 7.** Initial conditions of the tested cases in terms of subcooling degree ($\Delta T_{sub}$) and upstream pressure ($P_{up}/P_{cri}$). Three levels of subcooling are highlighted.

in fully liquid conditions, once the actual pressure and temperature in the pipe have been measured. The resulting relation reads:

$$c_{conf} = Ac_{free} = \frac{c_{free}}{0.96} \tag{4}$$

and shows that only a minor correction is needed to pass from $c_{conf}$ to $c_{free}$. Indeed this correction, derived in single-phase conditions, does not account for the compressibility effect. To include this effect we consider the Allievi formula

$$c_{free} = \frac{c_{conf}}{\sqrt{1-\mathcal{B}}} = \frac{c_{conf}}{\sqrt{1-\frac{\rho_{mix}c_{conf}^2 D}{eE}(1-\nu^2)}}, \tag{5}$$

with $D$ and $e$ the pipe diameter and thickness, $E$ the elasticity of the pipe, and $\nu$ the pipe Poisson ratio. $\rho_{mix}$ is the mixture density computed at saturation according to the homogeneous two-phase model, i.e. $\rho_{mix} = \alpha\rho_v + (1-\alpha)\rho_l$. The term $\mathcal$ is introduced In our experiments $\mathcal{B} << 1$, hence, also in a two-phase flow we will consider valid the approximation $c_{conf} \approx c_{free}$.

## 4. Results

This section is divided into three subsections. The first one describes the impact of the fluid initial conditions and subcooling level on cavitation, in terms of steady pressure and temperature. The second section focuses on the cavitation process itself, hence, on the pressure and temperature gradients measured through the orifice and on the final steady conditions measured downstream. Finally, the third section aims at characterizing, in detail, the different flow conditions. In particular, unsteady pressure measurements served to derive the speed of sound of the flow in the orifice far-field.

### 4.1. Initial conditions and subcooling level

A fine tuning of the pressure at the inlet of the orifice was achieved thanks to a pressurization unit consisting of a gaseous nitrogen bottle and pressure regulators. The subcooling degree, instead, could not be independently fixed since the facility did not include a preheating/precooling unit for the working fluid upstream of the orifice. Fig. 5 shows the full set of initial conditions of the experimental campaigns in a P-T diagram. These conditions are presented together with the saturation and the spinodal curve, and all fall in the metastable area between these two curves.

Most of them feature a common trend; the initial conditions with higher pressure are the furthest from the saturation curve, whereas the ones with lowest pressure are almost at saturation. Indeed, the subcooling degree changed by regulating the liquid pressure in the ranger. Few exceptions to this trend are also present and may be ascribed to the ranger initial conditions. Let us look at two specific cases highlighted in Fig. 6, which both have a similar $P_{up}$ and pressure drop, respectively, $\Delta P = 360$ and 330 kPa but have different subcooling levels. As for the case $C2$, which is closer to the saturation curve, the liquid reaches its final conditions in the region of the diagram where the fluid is considered to be in the vapor phase, i.e. below the saturation curve. Thus, we observe downstream of the orifice a fully developed cavitation with vapor filling the whole portion of the test section. On the contrary, for the $C1$ case, the pressure drop is not sufficient to bring the liquid below the saturation curve and cavitation is not observed. Hence, the flow regime through the orifice is highly dependent on the subcooling degree.

Considering the key role played by the subcooling, from now on, the experimental data are classified accordingly to it. Fig. 7 shows the map of the test initial conditions in terms of $\Delta T_{sub}$ and the non-dimensional upstream pressure $P_{up}/P_{cri}$, where $P_{cri} \approx 3400$ kPa. Three regions of subcooling have been defined. The region $S1$ corresponds to $\Delta T_{sub} < 0.020$, the region $S2$ groups the data with $0.02 < \Delta T_{sub} < 0.05$ and, finally, the region $S3$ includes the cases with $\Delta T_{sub} > 0.05$. This last region contains the points with higher upstream pressure ($P_{up} \sim 800$ kPa).

### 4.2. Steady-state flow analysis

Fig. 8 shows the pressure $P3$ and temperature $T3$ measured downstream of the orifice for all the inlet conditions.

The test cases for which cavitation has not been visually observed, lay on the upper part of the P-T diagram. In the lower part of the P-T diagram, and closer to the saturation curve, we find the test cases belonging to the regions $S2$ and $S3$. The furthest among them lie maximum at $\sim 2$ K from the saturation curve. On the other hand, the test cases belonging to the region $S1$ lie furthest from the equilibrium, and at a maximum distance of $\sim 6$ K.

To better explain this behavior, both the non-dimensional numbers $Rp$ and $\Delta T_{sat,\,dw}$ should be observed. Let us consider Fig. 9.

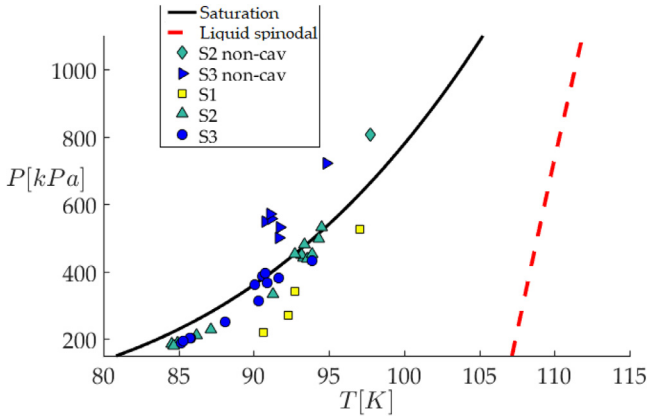


**Fig. 8.** Flow conditions ($P3$ and $T3$) at the outlet of the orifice and their relative position with respect to the saturation and the spinodal curve. Different symbols distinguish the cases $S1$, $S2$, and $S3$.

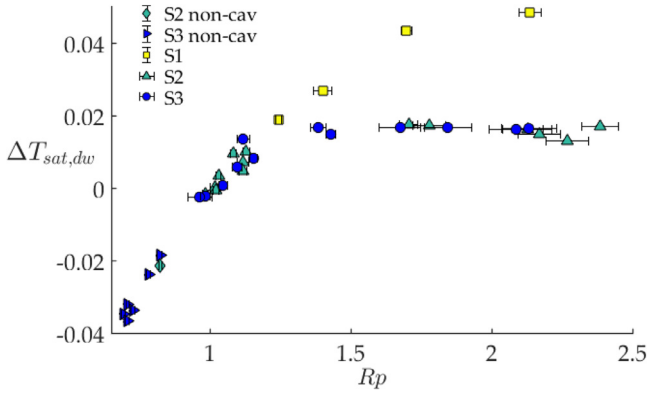


**Fig. 9.** Temperature distance from the equilibrium state downstream of the orifice as a function of Rp for all the tested cases.

First $\Delta T_{sat,\,dw}$ increases, almost linearly, with $Rp$ up to a value of $\Delta T_{sat,\,dw} \sim 0.02$ when $Rp \sim 1.2$. At that point two different behaviors are distinguished. The test cases corresponding to the regions $S2$ and $S3$ keep a constant $\Delta T_{sat,\,dw}$, whereas the ones corresponding to the region $S1$ present a further increase of $\Delta T_{sat,\,dw}$. In other words, test cases with higher initial subcooling (region $S2$ and $S3$) reach a thermodynamic condition, downstream of the orifice, close to saturation independently on the downstream pressure. On the contrary, if the fluid initial conditions are close to saturation (region $S1$), the highest the $Rp$, the farthest will be the fluid from the saturation condition.

Let us consider, now, the temperature drop through the orifice. As can be deducted from the conservation of energy, the temperature falls during cavitation. Indeed, the latent heat is extracted from the surrounding liquid in order to form and to sustain a vapor bubble. This temperature depression is more significant for cryogenic fluids [5,12], hence the need to consider the Jakob number.

Fig. 10 (a) shows the $Ja$ as a function of the $Rp$ for the test cases in which cavitation has been observed. Six tests are labeled and an example of their corresponding flow visualization is shown in Fig. 10(b).

When cavitation starts, at $Rp \approx 1$, the temperature does not significantly drop through the orifice, i.e. $\Delta T_{ori} = T_{up} - T_{dw} \approx 0$ and $Ja \approx 0$, and the flow downstream of the orifice is almost at equilibrium. The instantaneous image of the case 1 at $Rp \approx 1$ shows a weak cavitation with few bubbles shedding from the orifice and dissolving ~ 10 mm downstream. By increasing $Rp$, cavitation goes from a weak, case 1, to a foamy cloud which extends for a

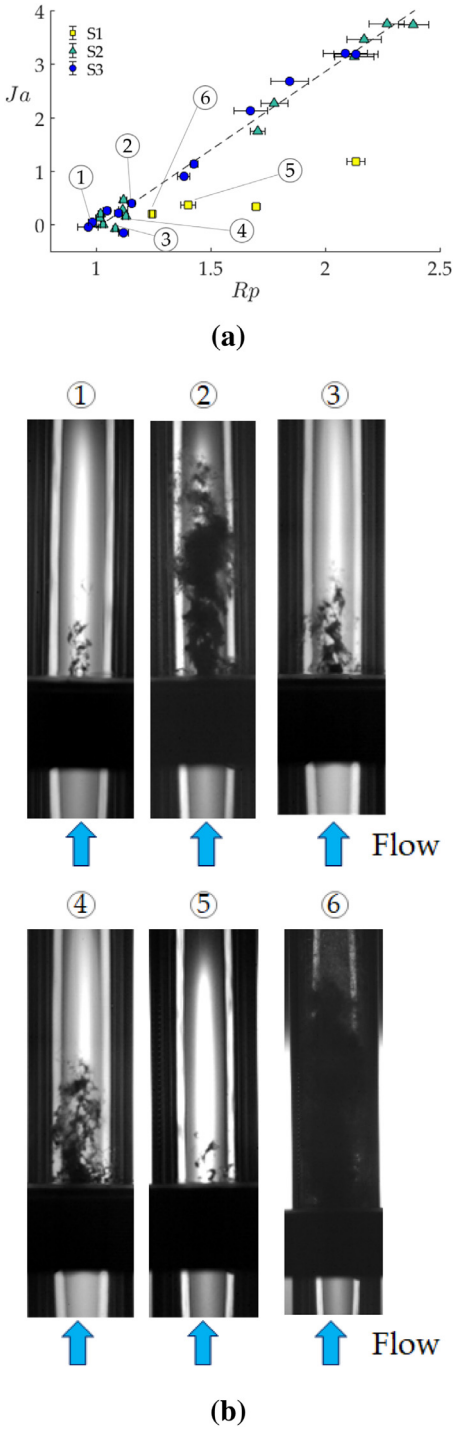


**Fig. 10.** (a) Variation of $Ja$ with respect to $Rp$ for the test cases in which cavitation has been observed. Six cases are highlighted and the corresponding instantaneous visualizations are shown (b).

length around 2D, cases 2. Cases 1 and 2 correspond to tests with $P_{up} \approx 800$ kPa and belong to the $S3$ group.

Lower subcooling ($S2$) and lower upstream pressure ($P_{up} \approx 640$ kPa) lead to a lower vaporization rate as the ones shown for case 3 and case 4. All the data with $Rp > 1.2$ present the highest vaporization rate and the visualized flows are similar to that of the case 6. The only exception is the case 5 which presents a cavitation regime similar to case 1. Unlike case 6, which is obtained at $P_{up} \approx 700$ kPa, case 5 corresponds to $P_{up} \approx 500$ kPa suggesting that

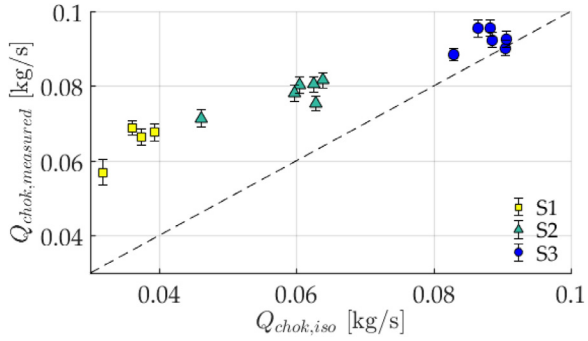


**Fig. 11.** Measured mass flow rate for the cavitation points with $Rp > 1.2$ against the theoretical $Q_{chok,iso}$.

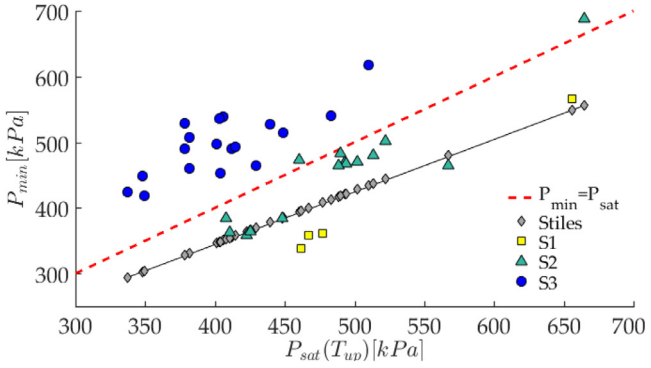


**Fig. 12.** Comparison between $P_{min}$ computed with the experimental correlations, Eqs. (10), (11), and $P_{min}$ according to Stiles' formulation, Eq. (7).

the upstream pressure effect cannot be neglected to determine the cavitating regime.

Globally, from Figs. 9 and 10 (a), two different behaviors are clearly observed as $Rp$ increases. For the test cases $S2$ and $S3$, the temperature drop through the orifice linearly increases with $Rp$. On the contrary, the temperature drop and the $Rp$ value seem to be uncorrelated for the cases belonging to the $S1$ region. This may be due to the higher energy and latent heat possessed by liquid when it is in subcooled conditions with respect to the saturated one. The $S1$ cases, having less energy, seem to spend most of their energy only to reach the required superheat level, remaining, thus, in a higher non-equilibrium state.

#### 4.2.1. Minimum pressure for the phase change

Although considering two different steps for the phase change is easier from a computational point of view, the vaporization process is unlikely to occur at the inlet temperature $T_{up}$ in non-isothermal conditions.

Therefore, as anticipated in [40], the common approximation $P_{min} \approx P_{sat}(T_{up})$ cannot be made. It becomes apparent when that approximation is used to compute the maximum flow rate ($Q_{chok}$) through the orifice as

$$Q_{chok,iso} = C_d A_o \sqrt{2\rho_l (P_{up} - P_{sat}(T_{up}))} \tag{6}$$

where $A_o$ is the orifice section, $\rho_l$ is the liquid density of the flow upstream of the orifice, and $C_d$ is the orifice discharge coefficient accounting for approximating the vena contracta section with the orifice one. A $C_d$ of 0.81 $\pm$ 0.02 was computed from the measured pressure drop and flow rate in fully liquid conditions, i.e $C_d = Q/(A_o\sqrt{2\rho_l \Delta P})$. The high vaporization produced during the tests at high $Ja$ and high $Rp$, see for example case 6 in Fig. 10(b), clearly indicates a choked flow. However, as shown in Fig. 11, the measured flow rates for such choked cases ($Q_{chok,measured}$) are higher than the ones computed using Eq. (6), especially for the tests belonging to the region $S1$ where the actual flow rate is almost twice the one calculated with Eq. (6).

A possibility to better predict the $P_{min}$ would be to assume $P_{min} = P_{sat}(T_{throat})$. In practice, $T_{throat}$ is hard to measure. Zhu et al. [41] and Ohira et al. [21] tried to overcome this issue by computing $T_{throat}$ as the average between the temperatures upstream and downstream of the nozzle, i.e. $T_{throat} = 0.5(T_{up} + T_{dw})$. In their studies $\Delta T_{ori} = T_{up} + T_{dw} \leq 0.5$, therefore, they suggest the error introduced by such an approximation can be considered small. Different is our case, where $\Delta T_{ori}$ up to 7.3 K are measured ($Ja \approx 3.7$).

Most likely, vaporization will occur at a pressure slightly lower than the saturation one because of the so-called metastability effects. In 1976, Stiles [42] modeled these effects by defining the liquid critical pressure ratio $F_f$ as:

$$F_f = 0.96 - 0.28\sqrt{\frac{P_{sat}}{P_{cri}}} \tag{7}$$

The minimum pressure $P_{min}$ to choke is then:

$$P_{min} = F_f \cdot P_{sat}(T_{up}) \tag{8}$$

This model provides $P_{min} << P_{sat}(T_{up})$ for those fluids whose $P_{sat}(T_{up})$ is closer to the critical point. However, the problem encountered with this model is that it underpredicts the maximum flow rate ($Q_{chok}$) through the orifice. Another interesting model was proposed by Aaron [43] who defined $P_{min}$ as a function of $P_{sat}(T_{up})$ and of several design parameters such as the upstream and downstream pressure, the initial degree of subcooling, and the length and diameter of the short tube geometry. Our approach follows Aaron's idea and is based on the experimental findings discussed in the previous sections. Since we observed a strong dependency of our results on $\Delta T_{sub}$ (Fig. 6) and on $Rp$ (Fig. 10),we use these two parameters to develop a simple semi-empirical model for the $P_{min}$. First, we compute the minimum pressure reached during cavitation using Eq. (6) and replacing $P_{sat}(T_{up})$ with $P_{min}$:

$$P_{min} = P_{up} - \frac{1}{2\rho_l}\left(\frac{Q_{chok}}{C_d A_o}\right)^2 \tag{9}$$

Then, we fit Eq. (9) with the experimental results using as parameters $P_{min}$, $P_{sat}(T_{up})$, $Rp$, and $\Delta T_{sub}$.

As seen in Fig. 9, $Rp$ seems to influence only the cavitating regime having higher subcooling (cases $S2$ and $S3$) where the fluid tends to the equilibrium. Consequently, we propose here two semi-empirical relations. One is valid for the cases with initial conditions $\Delta T_{sub} \geq 0.02$, i.e. the cases belonging to the regions $S2$ and $S3$, and this reads as :

$$\begin{aligned} P_{min} &= P_{sat}(T_{up})\mathcal{T}_{sub} = \\ &= P_{sat}(T_{up})\left[-0.18Rp^{0.87} + exp(\Delta T_{sub})^{4.97}\right] \\ &\quad for \quad \Delta T_{sub} \geq 0.020 \quad (R^2 = 0.991) \end{aligned} \tag{10}$$

The second correlation, instead, applies for the cases at saturation, that is $\Delta T_{sub} < 0.02$ in our case, and reads :

$$\begin{aligned} P_{min} &= P_{sat}(T_{up})\mathcal{T}_{sat} = P_{sat}(T_{up})\left[0.25(\Delta T_{sub})^{-0.27}\right] \\ &\quad for \quad \Delta T_{sub} < 0.020 \quad (R^2 = 0.980) \end{aligned} \tag{11}$$

The $P_{min}$ resulting from these correlations for all the tested points is shown in Fig. 12 and compared with the $P_{min}$ computed with Stiles' formulation, Eq. (7). The dashed line in the plot represents the condition $P_{min} = P_{sat}$. Following Stiles's model, the fluid reaches a minimum pressure below the saturation one and dependent on it. Therefore, all the experiments lay on the same line. A completely different distribution is observed by using the proposed correlations. Let us start considering the condition $P_{min} =$

**Table 1**
Characteristic parameters for the three flow conditions.

| | | $\sigma$ | $Rp$ | $Ja$ | $\Delta T_{sat,\,dw}$ |
|---|---|---|---|---|---|
| fully liquid | S1,S2,S3 | $> 1$ | $< 0.97$ | $\approx 0$ | $\leq 0.019$ |
| cavitation | S1,S2,S3 | $0.8 - 1$ | $0.97 - 1.2$ | $< 0.45$ | $0.027 \leq 0.013$ |
| flashing | S1,S2,S3 | $\leq 0.8$ | $> 1.2$ | $0.20 - 1.18$ | $0.019 - 0.048$ |
| | | | | $0.91 - 3.75$ | $0.013 - 0.017$ |

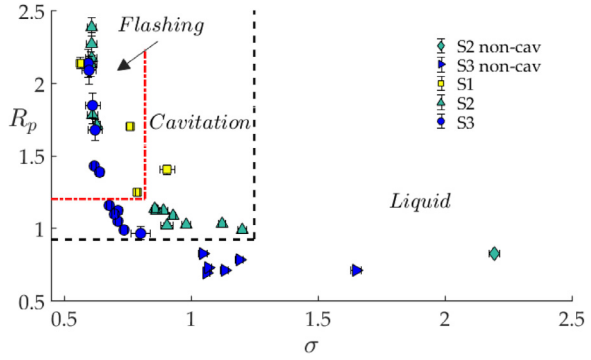


**Fig. 13.** Map of the tested cases in terms of Rp and $\sigma$ with highlighted the regions of different flow regime: fully liquid, cavitation, flashing.

$P_{sat}$. The closest points to this curve are those with $\Delta T_{sub} \approx 0.03$, i.e. $T_{sat}(P_{up}) - T_{up} = 5\,^{\circ}$C. For reducing $\Delta T_{sub}$, $P_{min} < P_{sat}$, meaning that the orifice chokes later than expected. Instead, at higher values of subcooling, i. e. cases S3, the minimum pressure is always higher than the saturation one. Despite the different fluid involved in the study and the geometry considered, this behavior is coherent with Aaron's results [43], according to which $P_{min} \approx P_{sat}$ for a subcooling of $\sim 5.6\,^{\circ}$C. As subcooling decreases, $P_{min} < P_{sat}$, whereas for subcooling higher than 5.6°C $P_{min} > P_{sat}$. As explained by Aaron, this last behavior means that the available subcooled pressure drop before the orifice chokes is smaller than the pressure drop induced by the orifice

When used to calculate $\sigma$, these two formulations yield a more meaningful and coherent comparison between the various test cases obtained with different $P_{up}$ and $\Delta T_{sub}$. In particular, we can now classify the different flow conditions in terms of $\sigma$ and $Rp$ as shown in Fig. 13, which highlights the three identified regions.

Single-phase flow takes place for $Rp < 0.97$ and $\sigma > 1$, and the inception of cavitation is firstly observed at $Rp = 1$ and $\sigma = 1.2$. When reducing $\sigma$ or increasing $Rp$, cavitation intensity increases up to reach the flashing if both $\sigma \leq 0.8$ and $Rp > 1.2$. The flashing is characterized by the highest rate of vaporization and the highest values of temperature drop, i.e. $Ja$ up to 3.7 for the $S2$ and $S3$ test cases. The characteristic parameters for the three flow regimes are summarized in Table 1.

### 4.3. Unsteady-state flow analysis

#### 4.3.1. Speed of sound measurements

Despite the lack of optical access at the three downstream pressure sensors location, Esposito et al. [39] reports that the global coherence function ($\gamma^2$) [35] can be considered a suitable indicator of the flow topology and it is defined as:

$$\gamma^2 = \frac{1}{2}\left[\gamma^2_{3,4} + \gamma^2_{5,4}\right] \tag{12}$$

where $\gamma^2_{3,4}$ and $\gamma^2_{5,4}$ are the coherence functions between P3 and P4 and between P5 and P4, respectively. A generic magnitude-

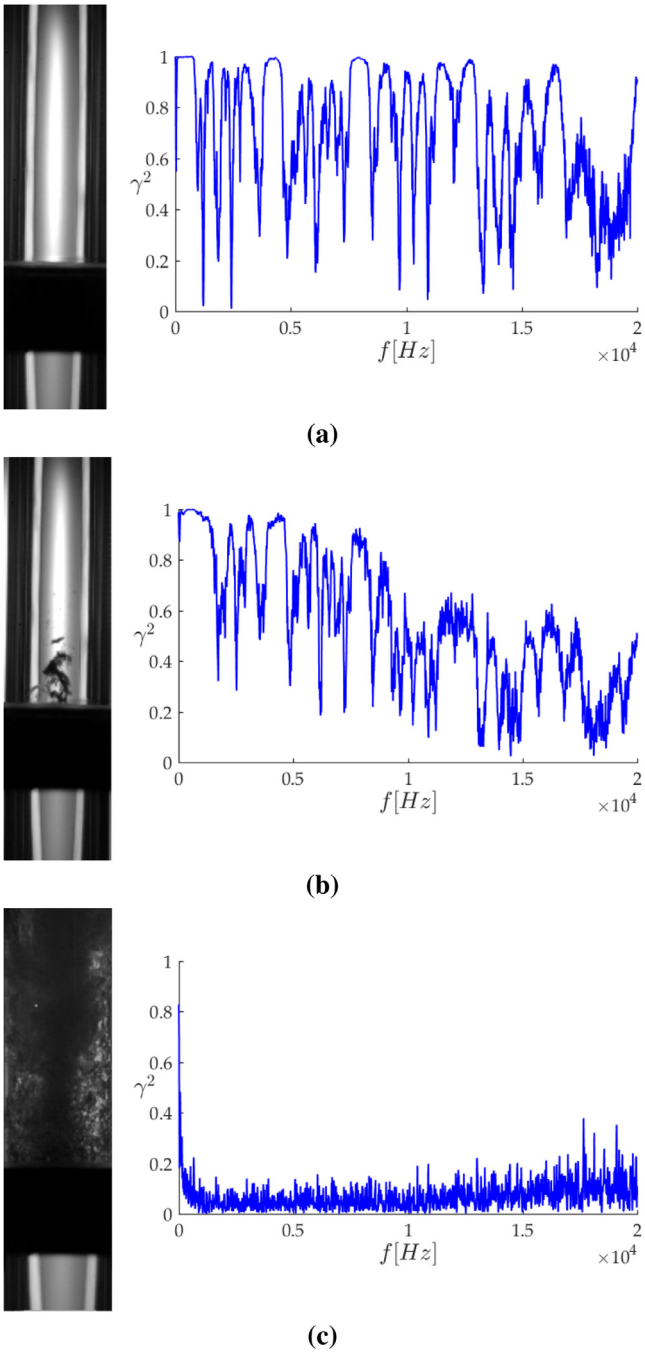


**Fig. 14.** Global coherence function for three test cases of the region $S3$ (high subcooling) and $P_{up} \approx 850$ kPa. **(a)** $\sigma = 1.06$, $R_p = 0.69$, and $Ja = 0$; (b) $\sigma = 0.74$, $R_p = 0.98$, and $Ja = 0.05$; (c) $\sigma = 0.59$, $R_p = 2.13$, and $Ja = 3.19$.

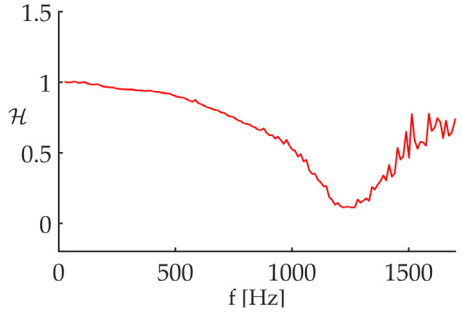


**Fig. 15.** Example of the obtained $\mathcal{H}$ in cavitating conditions with $Ja \approx 0$.

squared coherence function ($\gamma_{i,j}^2$) is given by

$$\gamma_{i,j}{}^2 = \frac{\left|G_{i,j}(f)\right|^2}{G_{i,i}(f) \cdot G_{j,j}(f)} \tag{13}$$

where $G_{i,j}$ is the cross-power spectral density, and $G_{ii}$ and $G_{jj}$ are the power spectral densities of each pressure signal. In order to derive the speed of sound for different flow conditions, we considered valid the pressure measurements at frequencies with a coherence $\geq 0.6$. This threshold guarantees a good coherence between the signals, ensuring anyway enough experimental points to correctly evaluate the first minimum of $\mathcal{H}$.

Let us first analyze three experimental cases and calculate the corresponding global coherence function $\gamma^2$ (Fig. 14). In fully liquid conditions, case (a), the global coherence function is well above the threshold for the entire considered frequency range, i.e. up to 20 kHz. Such a homogeneous flow results in the smooth $\mathcal{H}$ function shown in Fig. 3 with a first minimum located at 2 kHz. In presence of cavitation, Fig. 14(b), $\gamma^2$ starts to decrease when $f \geq 10$ kHz. This case corresponds to $\sigma = 0.74$, very small temperature drop across the orifice, $Ja = 0.05$, and to a downstream flow almost at equilibrium at $\sim T_{up}$. The corresponding $\mathcal{H}$ function, Fig. 15, becomes noisier already around 1500 Hz. Nevertheless, the first minimum shifts towards lower frequencies and it can still be clearly identified.

The last case, Fig. 14(c), presents a developed cavitation regime with high pressure and temperature drop across the orifice, i.e. $\sigma = 0.59$ and $Ja = 3.19$. The transparent test section is completely full of vapor and the coherence between the three pressure sensors in the far-field is completely lost, suggesting that the vapor cloud is extending in the pipe for at least 8 D downstream of the orifice, i.e. up to the location of $P3$. Thanks to the analysis of the whole set of tests, we have observed that a good flow homogeneity, i.e. $\gamma^2 \geq 0.6$ up to 10 kHz, was obtained for all the test cases with $Ja \leq 2$ independently on their subcooling level $\Delta T_{sub}$ and the value of $Rp$. Hence, a high level of vaporization along the pipe is driven by the temperature drop rather than the superheat level. Fig. 16 shows the results in terms of $M_l$ defined as the ratio of the velocity of the liquid upstream of the orifice ($U_l$) and the computed speed of sound $c_{free}$. As $\sigma$ decreases below 0.8, the 3PT technique measures a $c_{free}$ ranging between 435 and 530 m/s, that is $0.03 \leq M_l \leq 0.06$. The test cases with $Rp > 1.2$ and with a low $Ja$ present an even smaller $c_{free}$, ranging from 300 to 100 m/s. Nevertheless, a low $M_l$ below 0.3 is computed for all test cases. Concerning the $S1$ data, i.e. the yellow squares in Fig. 16, one may note that the point at $\sigma = 0.77$ seems to be uncorrelated to the others. Indeed, this test corresponds to the case 6 in Fig. 10, and, contrary to the other $S1$ cases, this is the only one with higher upstream pressure, i.e. $P_{up} \approx 700$ kPa. This difference suggests an impact of $P_{up}$, however, further investigation is required to draw general conclusions and to understand the individual role of each parameter ($P_{up}$ and $\Delta T_{sub}$).

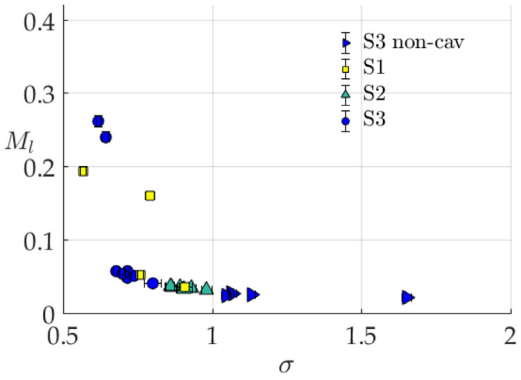


**Fig. 16.** Measured $M_l$ as a function of $\sigma$.

## 5. Conclusions

This paper discusses the influence of the fluid thermal properties on cavitation. For this purpose, we have investigated cavitation through an orifice using $LN_2$ as working fluid. The results have been analyzed in terms of five dimensionless numbers describing the flow conditions upstream ($\Delta T_{sub}$) and downstream ($Rp$, $\Delta T_{sat,\,dw}$) of the orifice, and the type of transition taking place through the orifice ($Ja$, $\sigma$). Besides, unsteady pressure measurements have been analyzed to further characterize the different flow conditions. The experiments have been grouped according to three levels of subcooling $\Delta T_{sub}$: $S1$ for $\Delta T_{sub} < 0.02$, $S2$ for $0.02 < \Delta T_{sub} < 0.05$, and $S3$ for $\Delta T_{sub} > 0.05$. When the liquid is further from the saturation, i.e. for the test cases belonging to the regions $S2$ and $S3$, it tends to rapidly restore a new equilibrium condition downstream of the orifice, independently on the value of the downstream pressure. To achieve that, the flow undergoes a temperature drop proportional to $Rp$. In other words, the thermodynamic effect appeared to increase when reducing $P_{dw}$ and increasing the pressure drop. On the contrary, when the fluid upstream of the orifice is close to saturation, it possesses less energy, and the two-phase flow downstream of the orifice is in a non-equilibrium state and is characterized by an almost isothermal phase change.

To compare the different cavitating conditions in terms of a cavitation number $\sigma$ which also takes into account the metastability of the flow, we have proposed a new model for the value of $P_{min}$ based on the experimental results. This model includes not only the $P_{sat}(T_{up})$ but also the subcooling degree $\Delta T_{sub}$ and the superheat level $Rp$ via the term $\mathcal{T}$. Indeed, these two parameters can significantly vary between different tests and the value of $P_{sat}(T_{up})$ was not able to provide a proper estimation of the minimum pressure reached at the orifice. This model allows a better comparison between the various test cases. Of course, despite giving satisfactory results for the tested orifice, the used correlations should be confirmed for different geometries and possibly with other fluids. Single-phase flows ($Rp < 0.97$ and $\sigma > 1$) are characterized by speeds of sound around $700 - 750$ m/s. The cavitation region is characterized by $Ja \approx 0$ and sees downstream of the orifice a drop of $\sim 200$ m/s of the speed of sound respect to the upstream conditions. Finally, flashing is characterized by the highest rate of vaporization and the highest values of temperature drop, i.e. $Ja$ up to 3.7 for the $S2$ and $S3$ test cases. Within this range, the 3PT was applicable only for $Ja < 2$ giving speeds of sound from 300 down to 100 m/s.

## Declaration of Competing Interest

None.

## Acknowledgments

This work is supported by the ESA's Networking/Partnering Initiative (NPI) grant 4000117725/16/NL/MH/GM and by the ESA's General Support Technology Programme (GSTP) contract 4000118113/NL/KML coordinated by Safran AeroBoosters.

## References

[1] V.H. Arakeri, V. Shanmuganathan, On the evidence for the effect of bubble interference on cavitation noise, J. Fluid Mech. 159 (1) (1985) 131, doi:10.1017/s0022112085003135.
[2] H. Ganesh, S.A. Mkiharju, S.L. Ceccio, Bubbly shock propagation as a mechanism for sheet-to-cloud transition of partial cavities, J. Fluid Mech. 802 (2016) 37–78, doi:10.1017/jfm.2016.425.
[3] J. Jakobsen, On the mechanism of head breakdown in cavitating inducers, J. Basic Eng. 86 (2) (1964) 291–305.
[4] J.-P. Franc, J.-M. Michel, Fundamentals of Cavitation, vol. 76, Springer Science & Business media, 2006.
[5] J.-P. Franc, C. Rebattet, A. Coulon, An experimental investigation of thermal effects in a cavitating inducer, J. Fluids Eng. 126 (5) (2004) 716–723, doi:10.1115/1.1792278.
[6] J. Hord, L. Anderson, W.J. Hall, Cavitation in Liquid Cryogens. 1: Venturi(1972).
[7] S. Watanabe, A. Furukawa, Y. Yoshida, Theoretical analysis of thermodynamic effect of cavitation in cryogenic inducer using singularity method, Int. J. Rotating Mach. 2008 (2008) 1–8, doi:10.1155/2008/125678.
[8] Y. Yoshida, K. Kikuta, S. Hasegawa, M. Shimagaki, T. Tokumasu, Thermodynamic effect on a cavitating inducer in liquid nitrogen, J. Fluids Eng. 129 (3) (2006) 273–278, doi:10.1115/1.2427076.
[9] J. Pinho, L. Peveroni, M. Vetrano, J.-M. Buchlin, J. Steelant, M. Strengnart, Experimental and numerical study of a cryogenic valve using liquid nitrogen and water, Aerosp. Sci. Technol. 93 (2019) 105331, doi:10.1016/j.ast.2019.105331.
[10] G. Mann, G. Madamadakala, S. Eckels, Heat transfer characteristics of R-134a in a converging-diverging nozzle, Int. J. Heat Fluid Flow 62 (2016) 464–473, doi:10.1016/j.ijheatfluidflow.2016.08.012.
[11] C. Mishra, Y. Peles, Development of cavitation in refrigerant (R-123) flow inside rudimentary microfluidic systems, J. Microelectromech. Syst. 15 (5) (2006) 1319–1329, doi:10.1109/jmems.2006.872230.
[12] N. Tani, T. Nagashima, Cryogenic cavitating flow in 2d laval nozzle, J. Therm. Sci. 12 (2) (2003) 157–161, doi:10.1007/s11630-003-0058-0.
[13] A. Hosangadi, V. Ahuja, Numerical study of cavitation in cryogenic fluids, J. Fluids Eng. 127 (2) (2004) 267–281, doi:10.1115/1.1883238.
[14] C.-C. Tseng, W. Shyy, Modeling for isothermal and cryogenic cavitation, Int. J. Heat Mass Transf. 53 (1–3) (2010) 513–525, doi:10.1016/j.ijheatmasstransfer.2009.09.005.
[15] K. Niiyama, S. Hasegawa, S. Tsuda, Y. Yoshida, T. Tamura, M. Oike, Thermodynamic effects on cryogenic cavitating flow in an orifice (2009).
[16] J. Zhu, D. Zhao, L. Xu, X. Zhang, Interactions of vortices, thermal effects and cavitation in liquid hydrogen cavitating flows, Int. J. Hydrogen Energy 41 (1) (2016) 614–631, doi:10.1016/j.ijhydene.2015.10.042.
[17] X. Long, Q. Liu, B. Ji, Y. Lu, Numerical investigation of two typical cavitation shedding dynamics flow in liquid hydrogen with thermodynamic effects, Int. J. Heat Mass Transf. 109 (2017) 879–893, doi:10.1016/j.ijheatmasstransfer.2017.02.063.
[18] C. Lee, T.-S. Roh, Flow instability due to cryogenic cavitation in the downstream of orifice, J. Mech. Sci. Technol. 23 (3) (2009) 643–649, doi:10.1007/s12206-008-1221-z.
[19] M.G.D. Giorgi, D. Bello, A. Ficarella, Analysis of thermal effects in a cavitating orifice using rayleigh equation and experiments, J. Eng. Gas Turbines Power 132 (9) (2010), doi:10.1115/1.4000367.
[20] M. Hitt, D. Lineberry, V. Ahuja, R. Frederick, Experimental investigation of cavitation induced feedline instability from an orifice, in: 48th AIAA/ASME/SAE/ASEE Joint Propulsion Conference & Exhibit, American Institute of Aeronautics and Astronautics, 2012, doi:10.2514/6.2012-4029.
[21] K. Ohira, T. Nakayama, T. Nagai, Cavitation flow instability of subcooled liquid nitrogen in converging–diverging nozzles, Cryogenics 52 (1) (2012) 35–44, doi:10.1016/j.cryogenics.2011.11.001.
[22] R. Xue, Y. Ruan, X. Liu, F. Cao, Y. Hou, The influence of cavitation on the flow characteristics of liquid nitrogen through spray nozzles: a CFD study, Cryogenics 86 (2017) 42–56, doi:10.1016/j.cryogenics.2017.07.003.
[23] T. Chen, H. Chen, W. Liu, B. Huang, G. Wang, Unsteady characteristics of liquid nitrogen cavitating flows in different thermal cavitation mode, Appl. Therm. Eng. 156 (2019) 63–76, doi:10.1016/j.applthermaleng.2019.04.024.
[24] T. Chen, H. Chen, W. Liang, B. Huang, L. Xiang, Experimental investigation of liquid nitrogen cavitating flows in converging-diverging nozzle with special emphasis on thermal transition, Int. J. Heat Mass Transf. 132 (2019) 618–630, doi:10.1016/j.ijheatmasstransfer.2018.11.157.
[25] H. Yoon, M. Ishii, S. Revankar, Choking flow modeling with mechanical and thermal non-equilibrium, Int. J. Heat Mass Transf. 49 (1–2) (2006) 171–186, doi:10.1016/j.ijheatmasstransfer.2005.07.044.
[26] E. Lauer, X. Hu, S. Hickel, N. Adams, Numerical modelling and investigation of symmetric and asymmetric cavitation bubble dynamics, Comput. Fluids 69 (2012) 1–19, doi:10.1016/j.compfluid.2012.07.020.
[27] S. Levy, D. Abdollahian, Homogeneous non-equilibrium critical flow model, Int. J. Heat Mass Transf. 25 (6) (1982) 759–770, doi:10.1016/0017-9310(82)90088-6.
[28] R.E. Henry, H.K. Fauske, The two-phase critical flow of one-component mixtures in nozzles, orifices, and short tubes, J. Heat Transf. 93 (2) (1971) 179–187, doi:10.1115/1.3449782.
[29] E. Goncalves, R.F. Patella, Numerical simulation of cavitating flows with homogeneous models, Comput. Fluids 38 (9) (2009) 1682–1696, doi:10.1016/j.compfluid.2009.03.001.
[30] J. Decaix, E. Goncalvès, Time-dependent simulation of cavitating flow with k-$\ell$ turbulence models, Int. J. Numer. MethodsFluids 68 (8) (2011) 1053–1072, doi:10.1002/fld.2601.
[31] S. Hickel, M. Mihatsch, S.J. Schmidt, Implicit large eddy simulation of cavitation in micro channel flows, arXiv preprint arXiv:1401.6548(2014).
[32] A. Šarc, T. Stepišnik-Perdih, M. Petkovšek, M. Dular, The issue of cavitation number value in studies of water treatment by hydrodynamic cavitation, Ultrason. Sonochem. 34 (2017) 51–59, doi:10.1016/j.ultsonch.2016.05.020.
[33] L. Peveroni, J. Steelant, M.R. Vetrano, Experimental investigation of liquid nitrogen chilldown two phase flow, in: Space Propulsion Conference, May 2-6, 2016, Rome, Italy, 2016.
[34] L. Peveroni, Y. Sakamoto, C. Fouchier, J. Steelant, J.-M. Buchlin, Liquid nitrogen chilldown: void fraction measurement and feasibility of extension to liquid methane testing, in: Space Propulsion Conference, May 14-15, 2018, Seville, Spain, 2018.
[35] H. Shamsborhan, O. Coutier-Delgosha, G. Caignaert, F.A. Nour, Experimental determination of the speed of sound in cavitating flows, Exp. Fluids 49 (6) (2010) 1359–1373, doi:10.1007/s00348-010-0880-6.
[36] D.L. Gysling, M.R. Myers, Distributed sound speed measurements for multiphase flow measurement, US Patent 6,813,962, 2004.
[37] D.L. Margolis, F.T. Brown, Measurement of the propagation of long-wavelength disturbances through turbulent flow in tubes, J. Fluids Eng. 98 (1) (1976) 70, doi:10.1115/1.3448215.
[38] Y. Sakamoto, L. Peveroni, H. Kobayashi, T. Sato, J. Steelant, J.-M. Buchlin, Void fraction measurement in cryogenic flows. part II: void fraction capacitive sensor performances in chilldown experiments, Cryogenics 96 (2018) 25–33, doi:10.1016/j.cryogenics.2018.10.002.
[39] C. Esposito, O. Yenigun, J.-B. Gouriet, J. Steelant, M.R. Vetrano, Void fraction and speed of sound measurement in cavitating flows by the three pressure transducers (3pt) technique, Exp. Therm. Fluid Sci. 112 (2020) 109949.
[40] L. Peveroni, C. Esposito, J. Pinho, J. Steelant, J.-B. Gouriet, Hydro-thermodynamic behavior of a hydraulic restriction in liquid nitrogen in steady-state and fluid-hammer conditions, in: Aerospace Europe Conference, February 25–28, 2020, Bordeaux, France, 2020.
[41] J. Zhu, H. Xie, K. Feng, X. Zhang, M. Si, Unsteady cavitation characteristics of liquid nitrogen flows through venturi tube, Int. J. Heat Mass Transf. 112 (2017) 544–552, doi:10.1016/j.ijheatmasstransfer.2017.04.036.
[42] G. Stiles, Cavitation and flashing considerations, in: ISA Handbook of Control Valves, 2nd Edition by Hutchinson, JW, 1976, pp. 206–211.
[43] D. Aaron, P.A. Domanski, An experimental investigation and modeling of the flow rate of refrigerant 22 through the short tube restrictor (NISTIR 89-4120), Technical Report, 1989.